Theoret. Comput. Fluid Dynamics (1991) 2: 307–317

Theoretical and Computational Fluid Dynamics

Propagating Structures in Wall-Bounded Turbulent Flows[1,2]

L. Sirovich

Center for Fluid Mechanics, Turbulence, and Computation, Division of Applied Mathematics, Brown University, Providence, RI 02912, U.S.A.

K.S. Ball

Department of Mechanical Engineering, The University of Texas at Austin, Austin, TX 78712, U.S.A.

R.A. Handler

Laboratory for Computational Physics and Fluid Dynamics, Naval Research Laboratory, Washington, DC 20375-5000, U.S.A.

Received 12 November 1990 and accepted 15 March 1991

Abstract. The Karhunen–Loève procedure is used to analyze two turbulent channel flow simulations. In both instances this reveals the presence of propagating plane wave structures in the turbulent flows. These waves appear to play an essential role in the local production of turbulence via *bursting* or *sweeping* events. The envelope of the propagating modes propagates with a speed which is equal to the mean velocity at the locus of maximal average Reynolds stress. Despite marked differences between the two flows similar results are obtained from each simulation. This is suggestive of the existence of universal or near universal features in the turbulent boundary layer. An analogy with critical layer mechanisms of transitional flows is discussed.

1. Introduction

Lumley (1967) suggested that the Karhunen–Loève (K–L) procedure (called by Loève (1955) the proper orthogonal decomposition) be used to extract *coherent structures* from turbulent flows. While its use for this purpose still needs further development the K–L procedure is without question an ideal means for analyzing the type of data obtained in turbulence experiments, both physical and computational. Lumley has further discussed and developed the method in two important publications (Lumley, 1970, 1981). A broad program for the use of the K–L procedure in turbulence problems was presented several years ago (Sirovich, 1987). Also the K–L procedure has been shown to be effective in producing a low-dimensional dynamical description of a model problem (Sirovich and Rodriguez, 1987). In this same vein, Lumley and coworkers (at Cornell) produced an interesting and provocative low-dimensional description, based on the K–L procedure, of wall-bounded turbulence (Aubry *et al.*, 1988; Armbruster *et al.*, 1988; Stone and Holmes, 1989). In the presentation given

[1] Dedicated to Professor J.L. Lumley on the occasion of his 60th birthday.

[2] We gratefully acknowledge support provided by DARPA-URI under Contract Number N00014-86-K0754. The use of the Pittsburgh Supercomputing Center is also acknowledged.

below we show that the empirical eigenfunctions that arise from the K–L procedure uncover some new phenomena in wall-bounded turbulence. In a recent paper (Sirovich *et al.*, 1990) we performed a K–L analysis on the dataset of a low Reynolds number turbulent channel flow. This analysis was shown to produce empirical eigenfunctions having the form of propagating plane waves. These waves form an evelope which travels at a velocity corresponding to the location where the Reynolds shear stress is a maximum. An analysis of the action of these propagating modes shows their importance in the initiation and development of bursting or sweeping events. The channel flow data which was analyzed was generated by a direct numerical simulation of the Navier–Stokes equations for a relatively coarse grain grid, with a Reynolds number $Re_\tau = 80$ based on the wall shear velocity, u_τ, and channel half-width, δ.

The present investigation further develops these ideas with the use of a similar analysis for a completely different and independent calculation carried out on a more highly resolved simulation at the higher Reynolds number $Re_\tau = 125$, and a different computational cell size. Both flows, while similar, are observed to have fundamental differences which are pertinent to our results and discussion. Nevertheless, the propagating structures occupy the same central role.

2. Background

The analytical approach for the study of turbulence and the dynamics of coherent structures which we follow is described by Sirovich (1987), and derives from Lumley's suggestion of using the eigenfunctions of the two-point velocity correlation tensor to decompose the flow into its relevant modes (Lumley, 1967, 1970, 1981). A complete and detailed discussion of the K–L decomposition, specifically applied to turbulent channel flows, is presented elsewhere (Ball *et al.*, 1991).

The channel flow simulations described in the next section take the flow to be periodic in the horizontal plane (x, z). As a result, the empirical eigenfunctions of the velocity correlation take the form

$$\mathbf{U}_{\mathbf{k}}^{(q)}(x, y, z) = \mathbf{V}^{(q)}(y; \mathbf{k})\mathbf{e}^{-i(k_1 x + k_3 z)} = \mathbf{V}_{\mathbf{k}}^{(q)}(y) \exp(-i\mathbf{k} \cdot \mathbf{x}), \tag{1}$$

where $\mathbf{k} = (k_1, 0, k_3)$ with $k_1 = 2\pi m/L_x$ and $k_3 = 2\pi n/L_z$. L_x and L_z represent the length of the computational domain in the streamwise and spanwise directions. The superscript, or quantum number, q, reflects the fact that for each $\mathbf{k}$ there is a hierarchy of modes. Thus the empirical eigenfunctions can naturally be regarded as *plane waves*, with propagation vector parallel to the bounding wall.

The projection of the flow, $\mathbf{u}(\mathbf{x}, t)$, along an eigenfunction (defined by the complex inner product) is

$$a_{\mathbf{k}}^{(q)}(t) = (\mathbf{V}_{\mathbf{k}}^{(q)}, \mathbf{u}) \tag{2}$$

which furnishes a time history of the mode and is itself the eigenfunction of the temporal correlation (Sirovich, 1987, 1991). Thus, if we represent the actual flow in terms of the empirical eigenfunctions,

$$\mathbf{u} = \sum_{q,\mathbf{k}} a_{\mathbf{k}}^{(q)}(t)\mathbf{V}_{\mathbf{k}}^{(q)} = \sum_{q,\mathbf{k}} \mathbf{v}_{\mathbf{k}}^{(q)}, \tag{3}$$

then $\mathbf{v}_{\mathbf{k}}^{(q)}$ has the form

$$\mathbf{v}_{\mathbf{k}}^{(q)} = b_{\mathbf{k}}^{(q)}(t)\mathbf{V}_{\mathbf{k}}^{(q)}(y)\mathbf{e}^{i(\omega_{\mathbf{k}}^{(q)} t - \mathbf{k} \cdot \mathbf{x})} \tag{4}$$

In writing $\mathbf{v}_{\mathbf{k}}^{(q)}$ in the form (4) we anticipate the secular trend in the phase of $a_k^{(q)}(t)$ which we find. Thus (4) is seen to be a propagating plane wave with direction determined by the wave number vector, $\mathbf{k}$. In (4), $b_{\mathbf{k}}^{(q)}(t)$ is the time-dependent portion of the coefficient $a_k^{(q)}$ which is left after the secular trend is removed. The actual phase or frequency of $a_{\mathbf{k}}^{(q)}$ is given by

$$\tilde{\omega}_{\mathbf{k}}^{(q)}(t) = \tan^{-1}\left(\frac{Im(a_{\mathbf{k}}^{(q)}(t))}{Re(a_{\mathbf{k}}^{(q)}(t))}\right), \tag{5}$$

while the value of $\omega_{\mathbf{k}}^{(q)}$ that appears in (4) is the linear fit to $\tilde{\omega}_{\mathbf{k}}^{(q)}$. Looking ahead to the results, the value of $\tilde{\omega}_{\mathbf{k}}^{(q)}$ is plotted as a dotted line in Figure 6, and in each case a linear trend is clear.

From (3) we see that the total mean energy in the flow is given by the sum

$$E = \langle(\mathbf{u}, \mathbf{u})\rangle = \sum_{q,\mathbf{k}} \lambda_{\mathbf{k}}^{(q)}, \tag{6}$$

where brackets denote an ensemble average, and where

$$\lambda_k^{(q)} = \langle (\mathbf{v}_k^{(q)}, \mathbf{v}_k^{(q)}) \rangle \tag{7}$$

are the energies in the corresponding (orthogonal) modes. The $\lambda_k^{(q)}$ may be shown to be the eigenvalues of the aforementioned velocity correlation operator. Thus, the eigenvalues provide a natural ordering for each mode in terms of its energy content.

3. Numerical Simulations

The steady-state turbulent velocity field for each of the two simulations was obtained by solving the Navier–Stokes equations in rotational form given by

$$\frac{\partial \mathbf{u}}{\partial t} = \mathbf{u} \times \boldsymbol{\omega} - \nabla\left(p + \frac{\mathbf{u}\cdot\mathbf{u}}{2}\right) + \frac{1}{R}\nabla^2\mathbf{u} + \mathbf{f} \tag{8}$$

subject to the incompressibility condition

$$\nabla\cdot\mathbf{u} = 0 \tag{9}$$

and the boundary conditions

$$\mathbf{u} = 0 \qquad \text{on} \quad y = \pm\delta; \tag{10}$$

$\mathbf{u}$ is the velocity, $\boldsymbol{\omega}$ is the vorticity, p is the pressure (divided by density), $R = 1/\nu$ (where ν is the kinematic viscosity), δ is the channel half-width, and $\mathbf{f}$ is a body force. This force is chosen to act like a constant pressure gradient which drives the flow to a statistically steady state.

The equations are solved using pseudospectral techniques in which Chebyshev polynomials are used in the wall normal direction and Fourier series are used in the streamwise, x, and spanwise, z, directions. That is, the velocity field is expanded in the following manner:

$$\mathbf{u}(\mathbf{x}, t) = \sum_{m=-M}^{M-1} \sum_{n=-N}^{N-1} \sum_{p=1}^{P} \tilde{\mathbf{u}}(m, n, p, t) \exp\left\{-2\pi i\left(\frac{mx}{L_x} + \frac{nz}{L_z}\right)\right\} T_p(y). \tag{11}$$

The details of the numerical methods used to solve the above equations for the datasets computed at $Re_\tau = 80$ are somewhat different from those used at $Re_\tau = 125$. The former was obtained by solving a fourth-order equation for the vertical velocity component and a second-order equation for the vertical component of vorticity. Since operator splitting is not employed in this method, continuity is satisfied exactly after each time step. Details of the method are described in the paper by Kim *et al.* (1987). An operator-splitting or time-splitting scheme is used to obtain the $Re_\tau = 125$ dataset. A Green's function approach developed by Marcus (1984) is used, which is a modification of the Orszag–Kells (1980) scheme in which time-splitting errors inherent in that method are significantly reduced by forcing a divergence free velocity field at the wall. Details of this latter method are given by Handler *et al.* (1989).

In Table 1 we summarize differences in resolution and channel dimensions for each simulation. The Reynolds numbers Re_c and Re_m, based on the full channel width 2δ and the centerline and mean velocities, respectively, are also tabulated. We note that in these low- and moderate-resolution

Table 1. Comparison of Computational Parameters.

Dataset	$Re_\tau = 80$	$Re_\tau = 125$
Resolution (x, y, z)	24 × 33 × 12	16 × 33 × 64
Re_c	3004	4256
Re_m	2419	3607
L_x (in wall units)	402	625
L_y (in wall units)	160	250
L_z (in wall units)	402	625
Re_c, Dean[15] correlation	2564	4246
Re_m, Dean[15] correlation	2190	3648

calculations, the streamwise length of the channel is not sufficiently long so that all two-point correlations decay to zero at streamwise separations less than the streamwise channel length. Thus in these two simulations, the largest flow structures do not completely decay or break up in the time it takes them to travel the length of the channel. As a consequence some care needs to be taken when interpreting time sequences of velocity data taken at a fixed spatial point since a single flow structure with sufficient coherence may appear at the observation point periodically.

The ability of such calculations to replicate natural turbulent flow in a channel thus depends on domain length and grid resolution. Inspection of Table 1 shows the domain used in the $Re_\tau = 125$ flow is considerably larger than the domain used in the $Re_\tau = 80$ flow. Thus, the effects of the periodicity of the domain should be less significant in the $Re_\tau = 125$ calculation.

Next, we note that the flow obtained from the $Re_\tau = 125$ calculation is considered *fully developed* in the sense described by Patel and Head (1969), while the flow at $Re_\tau = 80$ is considered *continuous*. Patel and Head concluded that for $Re_m > 2800$ the friction factor varied as the inverse one-sixth power of Re_m and for $Re_m > 3000$ the logarithmic layer of the mean velocity profile exhibited universal constants in the expression (Tennekes and Lumley, 1972)

$$u^+ = \kappa^{-1} \ln(y_+) + a. \tag{12}$$

u^+, in (12), represents the mean velocity normalized by the friction velocity, u_τ, and y^+ is the wall normal coordinate normalized by the wall scale (Tennekes and Lumley, 1972)

$$l_+ = \frac{\nu}{u_\tau}. \tag{13}$$

In these terms

$$Re_\tau = \frac{\delta}{l_+} \tag{14}$$

is the distance to the centerline in wall units.

We observe in Table 1 that Re_m for the $Re_\tau = 125$ calculation falls clearly in the fully developed range where a log-layer of universal character should be observed in the velocity profile. For the $Re_\tau = 80$ data, however, $Re_m < 3000$ and is also somewhat below the value for which a power-law relation between Re_m and the friction factor is observed. These experimental observations appear to be confirmed by the results shown in Figure 1 where we find a clear log-layer for the $Re_\tau = 125$ data, but none for the $Re_\tau = 80$ data.

In Table 1 we have computed Re_m and Re_c from the Dean (1978) correlation for the Reynolds numbers, Re_τ, represented by each simulation. That is, given an Re_τ (which is directly proportional to the driving mean pressure gradient), we use the experimental correlation of Dean to predict the mass

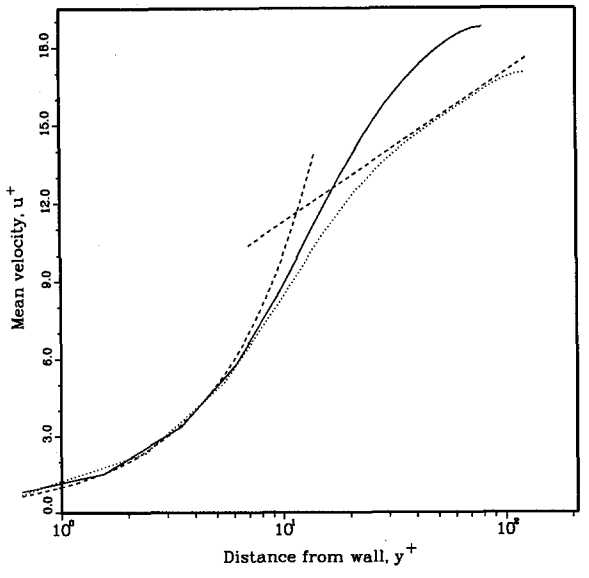

Figure 1. Mean velocity profile, u^+ (——, $Re_\tau = 80$; ·····, $Re_\tau = 125$; – – – –, law of the wall).

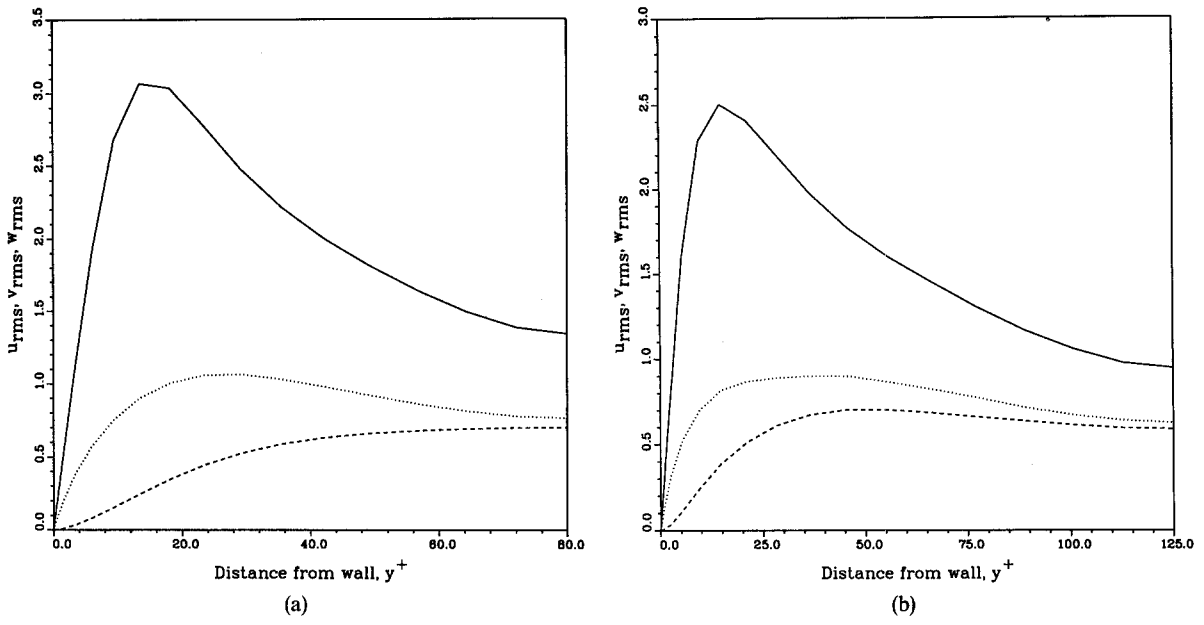

Figure 2. Root mean square velocity fluctuations; (a) $Re_\tau = 80$ and (b) $Re_\tau = 125$ (——, u_{rms}; – – – –, v_{rms}; ·····, w_{rms}).

flux through the channel. We see that the simulated and predicted values for Re_m and Re_c are in excellent agreement for the $Re_\tau = 125$ flow but that the Reynolds numbers obtained from the $Re_\tau = 80$ dataset are about 6% too large.

In Figure 2 we compare the root mean square (rms) velocity intensities from each simulation. We note that the peak in the intensity of the steamwise component of velocity occurs at a distance of about

$$y^+ \approx 14, \tag{15}$$

from the wall for each dataset, which is in excellent agreement with the experiments of Kreplin and Eckelmann (1979). As has been shown by Sreenivasan (1988) there is substantial evidence, over a range of Re, that u_{rms} always peaks at $y^+ \approx 14$. Also the turbulence production $-\langle uv \rangle du^+/dy$ appears to exhibit universal behavior and peaks at the same value of $y^+ \approx 14$ (Sreenivasan, 1988). (On considering the extremum of this quantity, we can show that it occurs at a location where the mean

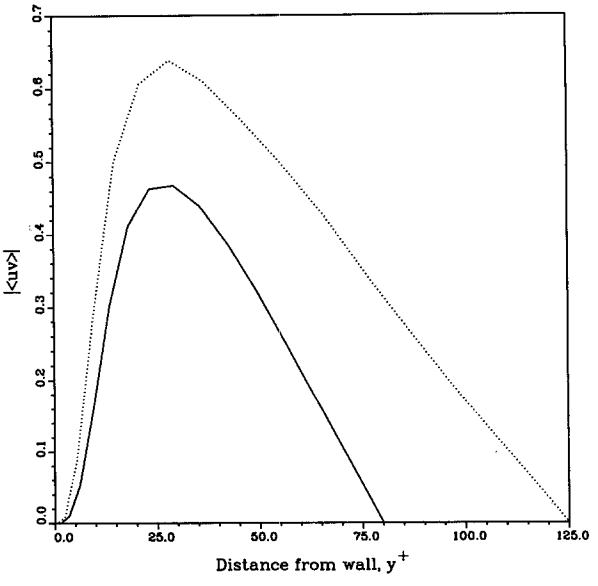

Figure 3. Mean Reynolds shear stress distribution (——, $Re_\tau = 80$; ·····, $Re_\tau = 125$).

velocity gradient du^+/dy is equal to $(du^+/dy)/2$ at the wall. This is located at $y^+ \approx 12$.) The spanwise and normal velocity components are also qualitatively similar, with broader peaks slightly further from the wall. These are known not to exhibit universal behavior, which is also clear from the simulations that are presented here.

In Figure 3 the mean Reynolds shear stress, $-\langle uv \rangle$, is shown for each simulation. The distribution of the Reynolds stress across the channel is qualitatively similar for both flows, with a fairly sharp and pronounced peak in the vicinity of $y^+ = 30$. This location of maximal Reynolds stress is consistent with the results of other studies (Kim *et al*, 1987; Eckelmann, 1974). (That the level of the Reynolds stress is lower for the case $Re_\tau = 80$ can be attributed to the lower intensity levels of the vertical velocity fluctuations in the near-wall region of the flow with $Re_\tau = 80$.) However, Sreenivasan (1988) has shown that a wide variety of experiments indicate that the location of peak Reynolds stress grows with Re_τ, as $O(Re_\tau^{1/2})$. Using an asymptotic argument, given in the Appendix, we can demonstrate that $-\langle uv \rangle$ peaks at

$$y^+ = \sqrt{\kappa^{-1} Re_\tau} \approx 1.58\sqrt{Re_\tau}. \tag{16}$$

This compares well with Sreenivasan's empirical formula of $y^+ = 2\sqrt{Re_\tau}$.

4. Empirical Eigenfunctions

The eigenvalue spectrum for each of the two flows being considered is shown in Figure 4. As discussed in Section 2, the total mean energy in the flow is given by the sum of the eigenvalues (6). Thus, each eigenvalue, $\lambda_{\mathbf{k}}^{(q)}$, gives the fraction of the total energy of the eigenfunction associated with it, $\mathbf{V}_{\mathbf{k}}^{(q)}$. By ordering the eigenvalues from largest to smallest, the number of eigenfunctions, N, needed to capture a given percentage of the total flow energy in a finite representation of the flow is minimized. The optimal nature of the energy convergence of the K–L expansion is well-known (Sirovich, 1989).

Each eigenfunction or mode is distinguished by its wave-number vector, $\mathbf{k}$, and quantum number, q. Table 2 provides a list of the energy content of the first 15 modes for each flow. (Recall m and n in Table 2 are defined by $k_1 = 2\pi m/L_x$ and $k_3 = 2\pi n/L_z$.) We note that the modes with zero wave number in the streamwise direction, $k_1 = 0$, collectively account for the most significant portion of the total energy in each flow. Additionally, the overwhelming majority of the most energetic modes individually have $k_1 = 0$ in each flow. The implications of this are discussed later.

In Figure 5(a) and (b) the y-dependence of the eigenfunction $\mathbf{V}_{13}^{(1)}$ is shown for $Re_\tau = 80$ and $Re_\tau = 125$, respectively. The spatial structure and symmetry properties of the empirical eigenfunctions in the channel flow geometry should be noted. We have chosen to present this particular mode

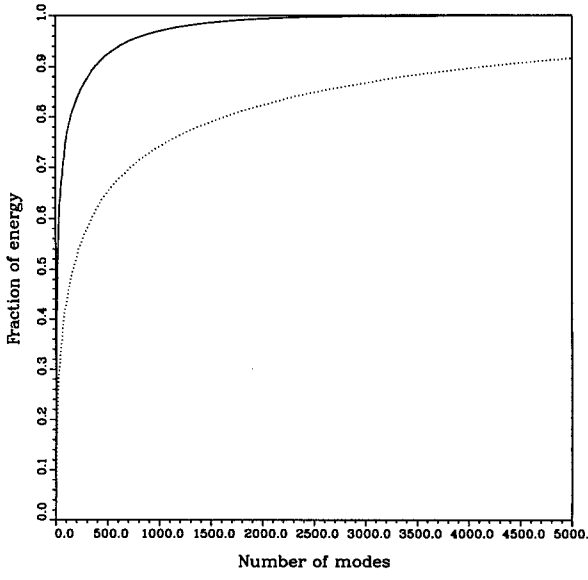

Figure 4. Energy convergence of the K–L expansion (——, $Re_\tau = 80$; ·····, $Re_\tau = 125$).

Table 2. Energy content of the first 15 eigenfunctions.

	$Re_\tau = 80$		$Re_\tau = 125$	
Index	(m, n, q)	Fraction of total energy	(m, n, q)	Fraction of total energy
1	(0, 1, 1)	0.1300	(0, 3, 1)	0.0428
2	(0, 2, 1)	0.0874	(0, 1, 1)	0.0399
3	(0, 3, 1)	0.0732	(0, 4, 1)	0.0327
4	(0, 2, 2)	0.0693	(0, 5, 1)	0.0287
5	(0, 1, 2)	0.0423	(0, 4, 2)	0.0229
6	(0, 3, 2)	0.0408	(0, 1, 2)	0.0210
7	(1, 3, 1)	0.0327	(0, 3, 2)	0.0206
8	(0, 0, 1)	0.0305	(0, 2, 1)	0.0197
9	(1, 3, 2)	0.0266	(0, 2, 2)	0.0188
10	(0, 1, 3)	0.0188	(0, 6, 1)	0.0138
11	(1, 2, 1)	0.0156	(0, 5, 2)	0.0131
12	(0, 0, 2)	0.0147	(1, 3, 1)	0.0125
13	(1, 2, 2)	0.0137	(1, 2, 1)	0.0095
14	(0, 1, 4)	0.0121	(1, 4, 1)	0.0084
15	(0, 2, 3)	0.0120	(1, 5, 1)	0.0083

because, in each case, it is the most energetic mode for which $k_1 \neq 0$ (see Table 2). It should be observed that the two cases have a different symmetry structure. In fact the (1, 3, 2) mode (not shown) at $Re_\tau = 80$ has the same form as the (1, 3, 1) mode of $Re_\tau = 125$. The (1, 3, 2) mode at $Re_\tau = 125$ has the same form as in Figure 5(a) and is 21st in the list. Thus a mode crossing has occurred.

A significant feature to observe in these figures is the strong peak in the streamwise component of the eigenfunction, $\mathbf{V}_u$, in the near-wall region $y^+ < 20$. In Figure 5(a) $\mathbf{V}_v$ exhibits more gradual variation through the channel, consistent with the form of the rms intensity of the vertical velocity component shown in Figure 2. Furthermore, the region of principal support for both eigenfunctions shown in Figure 5(a) and (b) corresponds to the location of the peak velocity intensities shown in Figure 2, which has obvious consequences in the representation of the Reynolds stress by the eigenfunction expansion (3).

The dynamical behavior of the mode $\mathbf{V}_{13}^{(1)}$ for each flow is shown in Figure 6(a) and (b). The time

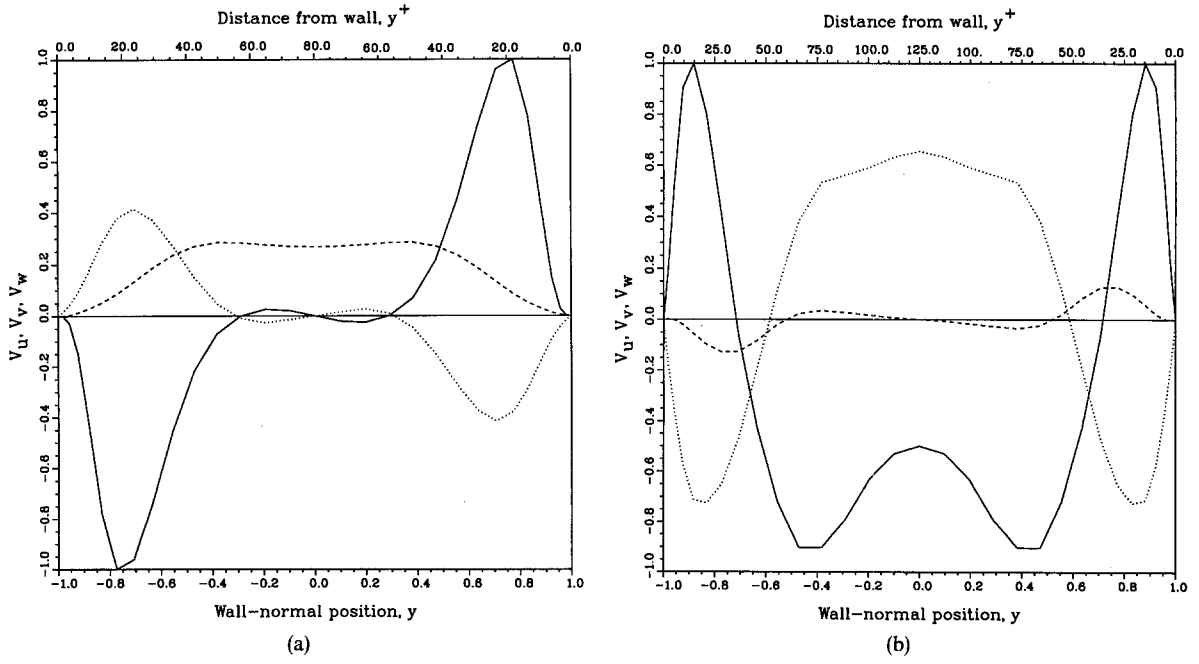

Figure 5. The spatial structure of the (1, 3, 1) eigenfunction: (a) $Re_\tau = 80$ and (b) $Re_\tau = 125$ (——, $\mathbf{V}_u$; – – – –, $\mathbf{V}_v$; ·····, $\mathbf{V}_w$).

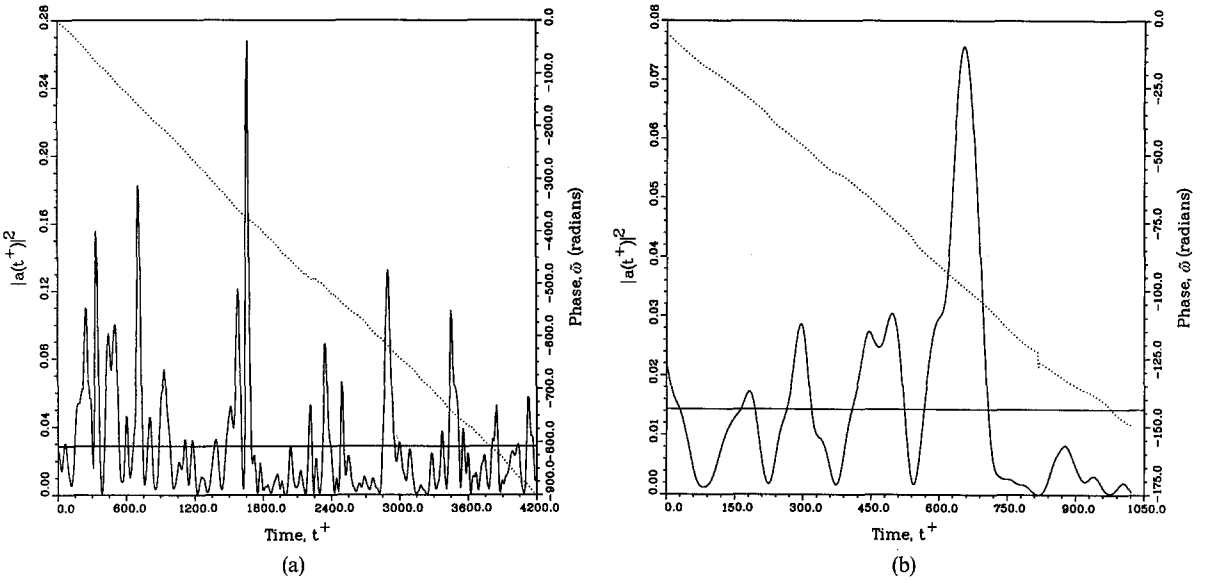

Figure 6. The time-series for the (1, 3, 1) eigenfunction: (a) $Re_\tau = 80$ and (b) $Re_\tau = 125$. The horizontal line is the eigenvalue for this mode (——, $|a(t^+)|^2$; ·····, $\tilde{\omega}$).

dependence of each mode is carried by the complex coefficient, $a_{\mathbf{k}}^{(q)}(t)$, which is defined by (2) and appears in the eigenfunction expansion (3). In these figures the mode activity is represented by the magnitude and phase of $a_{\mathbf{k}}^{(q)}(t)$, which supports the description of the empirical eigenfunctions as plane waves. The magnitudes for both flows exhibit a qualitatively similar, chaotic temporal behavior (note the finer time resolution for $Re_\tau = 125$ in Figure 6(b)). As follows from (4) and (7) the mean power for each mode is given by its eigenvalue

$$\langle |b_{\mathbf{k}}^{(q)}(t)|^2 \rangle = \langle |a_{\mathbf{k}}^{(q)}(t)|^2 \rangle = \lambda_{\mathbf{k}}^{(q)}, \tag{17}$$

which is also shown in the figure.

As mentioned earlier, in sharp contrast to the chaotic variation of the magnitude, the phase in both cases has a strong secular component resulting in a traveling wave, moving in the direction given by its wave-number vector. When differences in the channel dimensions between the two flows $Re_\tau = 80$ and $Re_\tau = 125$ are taken into account, the phase speeds for the $\mathbf{V}_{13}^{(1)}$ mode shown in Figure 6(a) and (b) are nearly identical. This is a fairly remarkable result, considering the many differences between the two datasets.

An examination of the complete set of eigenfunctions for each flow reveals that all modes which have a nonzero streamwise wave number also propagate with a characteristic velocity. (The modes with $k_1 = 0$ are nonpropagating and are termed kinematically degenerate (Sirovich *et al.*, 1990)). To picture how these plane waves move, we construct the normal speed locus. For this, the phase speed, $\omega_{\mathbf{k}}^{(q)}/|k|$, for each mode is plotted in the direction $\mathbf{k}/|\mathbf{k}|$. Figure 7(a) and (b) shows the normal speed locus for the flows $Re_\tau = 80$ and $Re_\tau = 125$, respectively, using the most energetic propagating modes (a greater number of modes has been included in Figure 7(b)). As can be seen the locus in each case is well approximated by a circle. The collection of the plane waves based on the normal speed locus generates an envelope which locates the most intense signal. (We mention in passing that the representation in terms of Chebyshev coefficients also exhibits wave propagation.)

The wave envelope follows by tracing a straight line perpendicular to the directions given by $\mathbf{k}/|\mathbf{k}|$ through each point of the locus. These lines are the tangents to the envelope. For the circular locus of Figure 7 this results in a single point on the k_1-axis, a distance from the origin equal to the diameter of the circle. It is found that the circles shown by the solid curves in Figure 7(a) and (b) yield, as the speed, the mean velocity at the same y^+ location where the Reynolds shear stress is a maximum (compare Figures 1 and 3)! The velocity scale is shown on the upper axis in Figure 7.

When we recall the structure of the eigenfunctions shown in Figure 5(a) and (b), we observe that

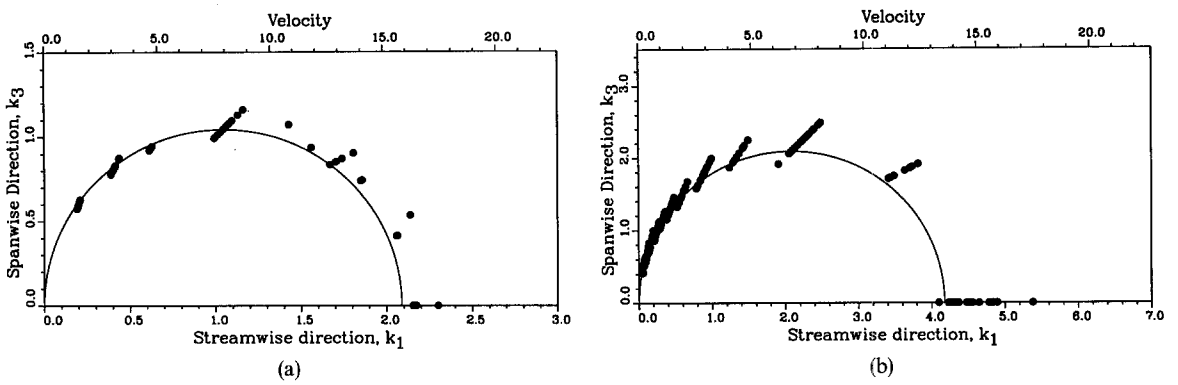

Figure 7. Normal speed locus: (a) $Re_\tau = 80$ and (b) $Re_\tau = 125$.

the eigenfunctions have their principal support in this same general location where $|\langle uv \rangle|$ is maximal. Thus, the plane wave modes are best able to extract energy from the mean flow via the Reynolds stress at this location, giving some basis as to why they propagate with the mean velocity at that location (see Section 5). We also note that as higher-order modes (with lower energy) are included in the construction of the locus, the degree of scatter increases. An examination of the spatial structure of these lower-energy modes reveals an increasing number of zero crossings, with a corresponding increased region of support. Indeed, as the mode energy becomes small, the eigenfunctions become in a sense locally sinusoidal. Consequently, they interact with the mean flow over a larger region of the domain, and are less likely to exhibit any particular characteristic velocity.

In Sirovich *et al.* (1990) we presented evidence that the propagating modes act as triggers for the *bursts and sweeps* that appear in wall-bounded turbulence (Willmarth, 1975a, b). This we briefly summarize here. First we write

$$\mathbf{u} = \mathbf{u}^s + \mathbf{u}^p, \tag{18}$$

where $\mathbf{u}^p$ is the summation over all propagating modes and $\mathbf{u}^s$ is the summation over all degenerate modes. We use the superscript s since these modes correspond to the streaky behavior found in turbulent boundary layers (Kline *et al.*, 1967). Roughly 75% of the energy of the (fluctuating part of the) flow resides in $\mathbf{u}^s$ and the remainder in $\mathbf{u}^p$, even though most modes are of the latter class. If we express the instantaneous Reynolds stress in these terms,

$$-uv = -u^p v^p - u^s v^s - \{u^p v^s + u^s v^p\}, \tag{19}$$

then we find:

(1) $u^s v^s$ is relatively small and slowly varying in time;
(2) $u^p v^p$ shows the same temporal behavior as uv but is extremely small;
(3) the cross term exhibits large temporal excursions, is relatively large itself, and has the temporal behavior of the full simulation.

Since $\mathbf{u}^p$ is essential for the recovery of the proper behavior of uv and since it is small we termed these propagating modes the triggers for burst and sweeps. They appear to ignite bursting and sweeping.

5. Remarks and Conclusions

Inspection of Table 2 shows that the most energetic mode for $Re_\tau = 125$ is (0, 3, 1) and hence it has three full waves in the z-direction. Moreover, from Table 1 we see that for $Re_\tau = 125$ the spanwise width of the computational cell is 625 wall units. Therefore the roll size of this mode is roughly 100 wall units, which is within the generally accepted range for the streak spacing (Sreenivasan, 1988). (For $Re_\tau = 80$ the situation is less clear.)

Over the years many other structural forms have been observed, e.g., large eddies (Townsend, 1966), hairpin vortices (Perry and Chong, 1982), transverse vortices (Praturi and Brodkey, 1978), and

so forth. The propagating modes introduced and discussed here are not necessarily independent of these, as these themselves are not necessarily independent of each other. We also note from Table 2 that the most energetic of the triggering modes propagates at roughly 70° from the downstream direction and the next most energetic at roughly 60°. In addition it is important to note that the wavelengths of these modes are more or less in resonance with the streak structures themselves.

We recall that Sreenivasan (1988) has suggested that the region in the neighborhood of peak Reynolds stress is analogous to the critical layer of transitional flow. The results of the present study support this notion. In fact the importance of the above-mentioned obliquely traveling waves is strongly reminiscent of the secondary instability which is essential to the transition process (Herbert, 1988; Bayly *et al.*, 1988).

One aspect of this picture, however, remains enigmatic. The location of maximal turbulence production, as stated earlier, appears to be universally fixed at $y^+ \approx 14$. This location we expect to be the source of the bursts and sweeps. However, the triggering mechanism is centered at $y^+ = 1.58\sqrt{Re_\tau}$ and hence moves away from $y^+ \approx 14$. (In physical units the actual location of (16) is $y/\delta = O(Re_\tau^{-1/2})$ which moves toward the wall.) Since the length-scale of the triggering mechanism is roughly 100 wall units, for $Re_\tau > 10^4$ the connection between the mechanisms becomes tenuous. It may of course be the case that at such high Reynolds numbers other mechanisms come into play.

We close by pointing out that the results of this study offer, at opposite extremes, some new possibilities for diminishing Reynolds stresses and enhancing the mixing process.

Appendix

The differential form of the mean momentum equation in the streamwise direction is

$$\frac{d}{dy^+}\langle uv\rangle = -\frac{1}{Re_\tau}\frac{d^2u^+}{dy_+^2}. \tag{A.1}$$

It should be emphasized that this is an exact expression. We verify, *a posteriori*, that $-\langle uv\rangle$ peaks for $y^+ \uparrow \infty$. Then, since (12) is valid in this limit, and for $Re_\tau \uparrow \infty$, the condition that $\langle uv\rangle$ be stationary yields

$$\frac{d^2}{dy^{+2}}\frac{1}{\kappa}\ln y^+ = 0. \tag{A.2}$$

This in turn yields (16). See Panton (1991) who has also obtained this result.

References

Armbruster, D., Guckenheimer, J., and Holmes, P. (1988). Heteroclinic cycles and modulated travelling waves in systems with $O(2)$ symmetry. *Phys. D*, **29**, 257.

Aubry, N., Holmes, P., Lumley, J.L., and Stone, E.J. (1988). The dynamics of coherent structures in the wall region of a turbulent boundary layer. *J. Fluid Mech.*, **192**, 115.

Ball, K.S., Sirovich, L., and Keefe, L.R. (1991). Dynamical eigenfunction decomposition of turbulent channel flow. *Internat. J. Numer. Methods Fluids*, **12**, 585.

Bayly, B.J., Orszag, S.A., and Herbert, T. (1988). Instability mechanisms in shear-flow transition. *Ann. Rev. Fluid Mech.*, **20**, 359.

Dean, R.B. (1978). Reynolds number dependents of skin friction and other bulk flow variables in two-dimensional rectangular duct flow. *J. Fluids Engrg.*, **100**, 215.

Eckelmann, H. (1974). The structure of the viscous sublayer and the adjacent wall region in a turbulent channel flow. *J. Fluid Mech.*, **65**, 439.

Handler, R.A., Hendricks, E.W., and Leighton, R.I. (1989). Low Reynolds number calculation of turbulent channel flow: A general discussion. NRL Memorandum Report 6410.

Herbert, T. (1988). Secondary instability of boundary layers. *Ann. Rev. Fluid Mech.*, **20**, 487.

Kim, J., Moin, P., and Moser, R. (1987). Turbulence statistics in fully developed channel flow at low Reynolds number. *J. Fluid Mech.*, **177**, 133.

Kline, S.J., Reynolds, W.C., Schaub, F.A., and Rundstadler, P.W. (1967). The structure of turbulent boundary layers. *J. Fluid Mech.*, **30**, 741.

Kreplin, H., and Eckelmann, H. (1979). Behavior of the three fluctuation velocity components in the wall region of a turbulent channel flow. *Phys. Fluids*, **22**, 1233.

Loève, M. M. (1955). *Probability Theory.* van Nostrand, Princeton, NJ.

Lumley, J.L. (1967). The structure of inhomogeneous turbulent flows. In *Atmospheric Turbulence and Radio Wave Propagation* (A.M. Yaglom and V.I. Tatarski, eds.), pp. 166–178. Nauka, Moscow.

Lumley, J.L. (1970). *Stochastic Tools in Turbulence.* Academic Press, New York.

Lumley, J.L. (1981). Coherent structures in turbulence. In *Transition and Turbulence* (R.E. Meyer, ed.), pp. 215–242. Academic Press, New York.

Marcus, P.S. (1984). Simulation of Taylor–Couette flow. Part I: Numerical methods and comparison with experiment. *J. Fluid Mech.*, **146**, 45.

Orszag, S.A., and Kells, L.C. (1980). Transition to turbulence in plane Poiseuille and Couette flow. *J. Fluid Mech.*, **96**, 159.

Panton, R.L. (1991). Scaling turbulent wall layers, *J. Fluids Engrg.*, **112**, 425.

Patel, V.C., and Head, M.R. (1969). Some observations on skin friction and velocity profiles in fully developed pipe and channel flows. *J. Fluid Mech.*, **38**, 181.

Perry, A.E., and Chong, M.S. (1982). On the mechanism of wall turbulence. *J. Fluid Mech.*, **119**, 173.

Praturi, A.K., and Brodkey, R.S. (1978). A steroscopic visual study of coherent structures in turbulent shear flow. *J. Fluid Mech.*, **89**, 251.

Sirovich, L. (1987). Turbulence and the dynamics of coherent structures, Part I: Coherent structures, Part II: Symmetries and transformations, Part III: Dynamics and scaling. *Quart. Appl. Math.*, **XLV** (3), 561–590.

Sirovich, L. (1989). Chaotic dynamics of coherent structures. *Phys. D*, **37**, 126.

Sirovich, L. (1991). Analysis of turbulent flows by means of the empirical eigenfunction. *Fluid Dynamics Res.* (in press).

Sirovich, L., and Rodriguez, J.D. (1987). Coherent structures and chaos: A model problem. *Phys. Lett. A*, **120**, 211.

Sirovich, L., Ball, K.S., and Keefe, L.R. (1990). Plane waves and structures in turbulent channel flow. *Phys. Fluids A*, **2**(12), 2217.

Sreenivasan, K.R. (1988). A unified view of the origin and morphology of the turbulent boundary layer structure. In *Turbulence Management and Relaminarization* (H.W. Liepmann and R. Narasimha, eds.), pp. 37–61. Springer-Verlag, New York.

Stone, E., and Holmes, P. (1989). Noise induced intermittency in a model of a turbulent boundary layer. *Phys. D*, **37**, 20.

Tennekes, H., and Lumley, J.L. (1972). *A First Course in Turbulence.* MIT Press, Cambridge, MA.

Townsend, A.A. (1966). The flow in a turbulent boundary layer after a change in surface roughness. *J. Fluid Mech.*, **26**, 255.

Willmarth, W.W. (1975a). Structure of turbulence in boundary layers. *Adv. Appl. Mech.*, **15**, 159.

Willmarth, W.W. (1975b). Pressure fluctuations beneath turbulent boundary layers. *Ann. Rev. Fluid Mech.*, **7**, 13.